RESEARCH ARTICLE

A novel tissue mechanics-based method for improved motion tracking in quasi-static ultrasound elastography

Niusha Kheirkhah[1] | **Sergio Dempsey**[1] | **Ali Sadeghi-Naini**[2,3] | **Abbas Samani**[1,4,5]

[1]School of Biomedical Engineering, Western University, London, Ontario, Canada

[2]Department of Electrical Engineering and Computer Science, York University, Toronto, Ontario, Canada

[3]Department of Radiation Oncology and Physical Sciences Platform, Sunnybrook Health Sciences Centre, Toronto, Ontario, Canada

[4]Departments of Medical Biophysics, Western University, London, Ontario, Canada

[5]Department of Electrical and Computer Engineering, Western University, London, Ontario, Canada

Correspondence
Abbas Samani, Departments of Medical Biophysics, Western University, London, ON , Canada, N6A 5C1.
Email: asamani@uwo.ca

Abstract

Purpose: Most cancers are associated with biological and structural changes that lead to tissue stiffening. Therefore, imaging tissue stiffness using quasi-static ultrasound elastography (USE) can potentially be effective in cancer diagnosis. USE techniques developed for stiffness image reconstruction use noisy displacement data to obtain the stiffness images. In this study, we propose a technique to substantially improve the accuracy of the displacement data computed through ultrasound tissue motion tracking techniques, especially in the lateral direction.

Methods: The proposed technique uses mathematical constraints derived from fundamental tissue mechanics principles to regularize displacement and strain fields obtained using Global Ultrasound Elastography (GLUE) and Second-Order Ultrasound Elastography (SOUL) methods. The principles include a novel technique to enforce (1) tissue incompressibility using 3D Boussinesq model and (2) deformation compatibility using the compatibility differential equation. The technique was validated thoroughly using metrics pertaining to Signal-to-Noise-Ratio (SNR), Contrast-to-Noise-Ratio (CNR) and Normalized Cross Correlation (NCC) for four tissue-mimicking phantom models and two clinical breast ultrasound elastography cases.

Results: The results show substantial improvement in the displacement and strain images generated using the proposed technique. The tissue-mimicking phantom study results indicate that the proposed method is superior in improving image quality compared to the GLUE and SOUL techniques as it shows an average axial strain SNR and CNR improvement of 44% and 63%, and lateral strain SNR and CNR improvement of 130% and 435%, respectively. The results of the phantom study also indicate higher accuracy of displacement images obtained using the proposed technique, including improvement ranges of 7–84% and 26–140% for axial and lateral displacement images, respectively. For the clinical cases, the results indicate average improvement of 48% and 64% in SNR and CNR, respectively, in the axial strain images, and average improvement of 40% and 41% in SNR and CNR, respectively, in the lateral strain images.

Conclusion: The proposed method is very effective in producing improved estimate of tissue displacement and strain images, especially with the lateral displacement and strain where the improvement is highly remarkable. While the method shows promise for clinical applications, further investigation is necessary for rigorous assessment of the method's performance in the clinic.

KEYWORDS
breast cancer, lateral displacement, lateral strain, motion-tracking, ultrasound elastography

1 | INTRODUCTION

Breast cancer is the second most diagnosed cancer in women, estimated to affect one in eight American women during their lifetime. It is estimated that in 2022, 43,250 women will die from breast cancer in the United States.[1] Vital to successful treatment of the patient, early detection achieved through regular breast cancer screening has shown to reduce mortality rate by 25% in the first 10 years where treating stage 1 cancer has the highest survival rate.[2,3] The motivation of this work is to improve the state-of-the-art of imaging technology developed for early detection of breast cancer where the focus is quasi-static ultrasound elastography (USE). The most common medical imaging technique used for breast cancer screening is X-ray mammography. However, due to ionizing radiation, the frequency of testing using this method is restricted, potentially delaying critically needed early diagnosis. Another concern of this screening method is that it is influenced by breast density and hormone replacement therapy, hence impacting its sensitivity for breast cancer detection, especially with young women with dense breasts where reported sensitivities are as low as ∼60%.[4,5]

When X-ray mammograms are inconclusive, B-mode ultrasound (US) imaging and magnetic resonance imaging (MRI) are used. While B-mode US is widely available and inexpensive, image quality is a limiting factor that impacts its sensitivity and specificity. Being highly sensitive, MRI is very effective for abnormality detection. However, its high cost and limited availability has ruled out its routine utility for early detection. As such, researchers have been actively working to develop affordable imaging techniques with high sensitivity and specificity. One promising option toward this goal is elastography[6–8] where maps of tissue stiffness are generated and visualized. In the context of breast cancer, this is motivated by the fact that many types of cancer, including ductal carcinoma which is the most common type of breast cancer, is associated with biological changes that lead to tissue stiffening.[9–12] As such, breast tissue stiffening may be evaluated for breast cancer detection. Among elastography techniques, quasi-static USE has been shown to be effective in stiffness imaging for a wide range of oncology applications, including breast, prostate and liver cancers.[13–18] Sensitivity and specificity of USE are reported at 88% and 83%, respectively. Benefits of USE include involvement of the noninvasive low-cost US imaging, being free of pain and harmful radiation, and fast data acquisition and image reconstruction.

In quasi-static elastography, a low frequency external loading is applied for tissue mechanical stimulation by pressing the US probe against the breast. US radiofrequency (RF) data is then acquired during tissue compression whereby an RF data frame is collected at each time instant of compression. Using two RF data frames corresponding to two compression states, the tissue displacement data can be estimated.[6,19–21] The tissue strain image calculated by differentiating the displacement field is considered the simplest form of elastography which is often integrated into US systems for real-time imaging.[6] Assuming tissue stress uniformity, strain images generated through this method can be regarded as an approximation to tissue stiffness maps (e.g., hard lesions appear as low strain areas). While strain imaging has been shown to be useful for some clinical applications,[8,20–22] due to the weakness of stress uniformity assumption, its accuracy in mapping tissue stiffness is limited. As such, more advanced techniques have been developed to image more reliable measures of tissue stiffness (e.g. Young's modulus) using the measured displacement field.[13,53,61,62]

In both strain imaging and Young's modulus imaging, the primary determining factor of accuracy is the accuracy of the tissue displacement data consisting of axial and lateral displacement fields. Young's modulus image reconstruction involves an ill-posed inverse problem. This issue can be mitigated if reliable estimates of both axial and lateral displacement components are available. While existing tissue motion tracking methods provide accurate estimation of tissue axial displacement, methods are yet to be developed for accurate estimation of the lateral component of tissue displacement. Several methods exist to estimate axial and lateral displacements using US RF data; however, the low signal-to-noise (SNR) ratio, limited resolution and lack of phase information in the lateral direction of ultrasound signals in addition to the errors associated with the 2D nature of conventional US imaging, pitch size, beam width, and interpolation applied to RF samples, have limited the accuracy of estimated displacements, especially the lateral displacement component. This has encouraged efforts toward development of more robust methods for displacement estimation. Estimation of tissue displacement and strain distribution in USE can be considered as an optical flow (OF) problem, which involves minimization of an energy equation imposing both echo amplitude conservation and displacement smoothness constraints.[23–27] More recently, deep learning methods were proposed for displacement and strain estimation that have proved promising.[28–30] Other algorithms mostly focus on time delay estimation (TDE) methods[19,30–37] where the TDE can be obtained for small windows of RF data. TDE involves a search which can be performed in either 1D or 2D corresponding to search in the axial direction only or in both lateral and axial directions, respectively.[36,37] While they generally provide accurate estimate in the axial direction, these approaches are too sensitive to signal decorrelation which often occurs in clinical breast imaging. To alleviate the decorrelation problem and improve the lateral displacement estimation, recorrelation methods have been proposed such as those based on aligning

and stretching RF signal.[64–67] However, these methods are vulnerable to speckle noise and are associated with relatively high computational cost.[68,69] Another effective approach followed to develop a robust method against signal decorrelation involves optimization constrained by regularization which imposes smoothness of tissue deformation.[31,32] In this approach, the displacement is estimated along a single RF-line, leading to displacement discontinuity between adjacent RF-lines and low accuracy of the lateral displacement field.[31] To avoid this, the displacement estimation can be performed simultaneously for all RF lines.[32] This method leads to excessively smooth displacement field, hence blurry strain images. To address this issue, a window-based term in conjunction with first or second order derivative based regularization were employed in other relevant works considered the state-of-the-art methods in this field.[33,38] A number of other studies have investigated utilizing more than two RF frames to estimate the displacement fields.[34,39–42] The basis of these motion-tracking methods is optimizing a cost function where a displacement continuity assumption is combined with echo signal correlation and other regularization terms. One downside of this approach is the necessity of appropriately determining the weighting coefficients of the terms in the cost function. In another category of displacement estimation methods, known as quality-guided motion tracking,[43–47] the displacements are first estimated for points in high correlation local regions before they are estimated for points in low correlation local regions. In addition to being computationally more efficient, this method has shown to operate well in regions with poorly correlated RF data and also geometrically irregular regions.[45]

While the above motion tracking methods can produce reasonably accurate axial displacement maps, the accuracy of their lateral displacements are generally low. At their core, these techniques rely on regularization through imposing tissue continuity and various field smoothness criteria. Utilizing tissue mechanics constraints such as incompressibility, compatibility and tissue 3D deformation models have not been as rigorously investigated for formulating more effective regularization to find more accurate 2D displacement fields. As an attempt to incorporate such constraints towards improved displacement estimation, approximate tissue mechanics-based relations founded on the stress uniformity assumption were derived and incorporated in an algorithm that uses three US RF frames.[39] Efforts have been also made to utilize the partial differential equations governing the linear elastic deformation in soft tissue. This includes a method proposed to estimate tissue lateral displacement field using measured axial displacement field based on tissue incompressibility condition.[48] The method assumes plane strain conditions, and it was shown that the estimated lateral displacement field was more accurate as it showed SNR improvement of up to 16.0 compared with a field estimated using traditional speckle tracking. The method was then extended to account for large deformation conditions under plane strain assumption.[49] Also through assuming plane strain conditions, a nearly incompressible constraint was used as a regularization term in a pixel-wise model-based algorithm to estimate all components of vascular strain (axial, lateral, and shear) with a sub-pixel resolution.[50] Tissue incompressibility constraint has also been used in other methods by incorporating confidence weights for different tissue regions and momentum conservation equation in conjunction with a robust H_∞ filter.[51,52] More recently, a mathematical framework was developed to improve an estimate of tissue axial and lateral displacement fields while the shear modulus was also reconstructed simultaneously.[53] The framework assumes plane stress and tissue incompressibility conditions while it does not require traction or displacement boundary conditions.

In this paper, we introduce a novel algorithm that uses a tissue mechanics-based estimation of out-of-plane strain to improve the in-plane tissue displacement and strain fields. Unlike previous studies, the proposed method does not assume plain strain or plane stress conditions and it uses Boussinesq's analytical model to estimate the out-of-plane strain before its incorporation in the incompressibility constraint. Another novelty of the method is enforcement of tissue deformation compatibility to improve tissue strain estimates.[60] Improving the accuracy of enforcing tissue incompressibility and deformation compatibility has been demonstrated to be highly effective in obtaining more accurate estimates of displacement and strain fields, especially their lateral components. Such improvement is anticipated to have a tangible impact on the accuracy of tissue stiffness parameter reconstruction using quasi-static elastography techniques.[13,53,61,62]

2 | MATERIALS AND METHODS

2.1 | Overview of the Strain Refinement Algorithm (STREAL)

The proposed algorithm requires an initial estimate of the displacements to be processed before an improved estimate is generated. To obtain an initial estimate of the tissue axial and lateral displacement fields, we process a suitable pair of acquired RF data frames using existing algorithms such as those developed based on the Global Ultrasound Elastography (GLUE) or Second-Order Ultrasound eLastography (SOUL) methods.[31,32,38] These methods formulate the displacement estimation associated with all samples of RF data simultaneously in a form of nonlinear optimization problem with first-order or second-order regularization constraints that are solved after conversion to a sparse
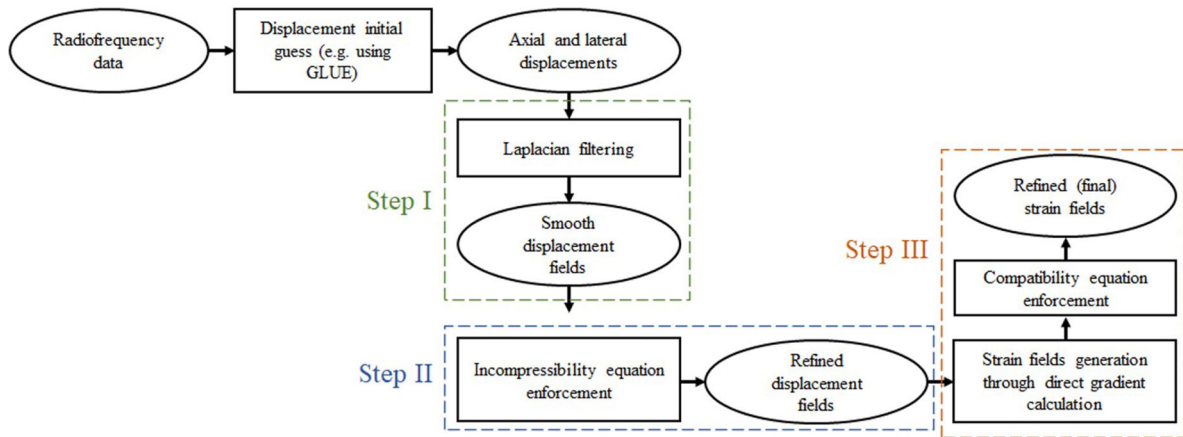
FIGURE 1 Schematic diagram illustrating the proposed step-by-step STREAL algorithm

linear system of equations. The initial estimates of displacement fields are then refined step-by-step through the proposed algorithm (STREAL) by first smoothing and then enforcing the fundamental tissue mechanics conditions of incompressibility and compatibility. The smoothing and incompressibility condition enforcement leads to improved displacement fields estimate while the compatibility condition enforcement applied to the strain fields leads to further improvement of the strain fields. This has been illustrated in Figure 1.

2.1.1 | Step 1: Second-Order Derivative-Based Regularization

In this step of regularizing the initial displacement data, we use a regularization method, which seeks a new estimate of the displacement field where the 2D Laplacian of the displacement components throughout the field of view (FOV) is minimized. The 2D-Laplacian of the displacement field U is expressed mathematically by:

$$\nabla U(x, y) = \partial^2 U(x, y) / \partial x^2 + \partial^2 U(x, y) / \partial y^2 \quad (1)$$

In this equation, x and y refer to the lateral and axial directions, respectively. This operator can be expressed in a matrix form by applying the finite difference approximation of this operator to each point in the FOV except points located on the FOV outline, leading to the following matrix form:

$$\nabla U(x, y) = LU \quad (2)$$

where L is a matrix with entries of the finite difference coefficients of the Laplacian operator and U is a 1D vector containing both axial and lateral displacement fields. The entries of L are arranged such that each row of Equation (2) yields the finite difference approximation of the Laplacian operator at each point. The solution sought in this step is the one that min-

imizes the Laplacian while it matches the input initial displacement field (U_m) obtained from any available tissue displacement tracking technique as much as possible. This leads to the following minimization equation of Tikhonov regularization:

$$Min. \left(\|U - U_m\|^2 + \lambda^2 \|LU\|^2 \right) \quad (3)$$

where $\| \cdot \|$ represents the Euclidean norm and λ^2 represents a positive weight coefficient. This minimization leads to the following least squares solution:

$$U_{new} = \left(I + \lambda^2 L^T L \right)^{-1} U_m \quad (4)$$

It is noteworthy that other than the Laplacian, there are also other choices that can be used for smoothing the displacement field. They include lower order or higher order derivative operators. The advantage of the Laplacian operator is its low cost in addition to its high effectiveness for tissue motion tracking.[38] The regularization weight coefficient, λ, determines the level of smoothness. This coefficient is found automatically using the L-curve technique[54] where a solution U is found for various λ values before $\|LU\|$ is plotted against $\|U - U_m\|$. Typically, this plot resembles L-curve, and the knee point of this curve corresponds to a λ value that is considered optimal as it corresponds to the best trade-off between smoothness and original data matching.

2.1.2 | Step 2: Tissue Incompressibility Enforcement

Tissue incompressibility is expressed mathematically by setting the divergence of the displacement field in 3D to zero as follows:

$$\nabla \cdot U(x, y, z) = \partial u_x / \partial x + \partial u_y / \partial y + \partial u_z / \partial z = 0 \quad (5)$$

where in the context of US image coordinate system, x, y, and z correspond to the lateral, axial, and out-of-plane directions, respectively, and u_x, u_y, and u_z are the displacement components in these directions, respectively. Since conventional US data does not provide information on the out-of-plane displacements, assumptions such as plane-strain and plane-stress have been used as discussed in the introduction. Assuming plane-strain conditions, in which the out-of-plane strain is zero, the incompressibility condition leads to the following equation:

$$\partial u_x/\partial x + \partial u_y/\partial y = 0 \qquad (6)$$

The plane strain assumption considered in previous works, however, is not valid in breast USE, as it requires ideal conditions of constant section geometry and uniform loading of tissue along the z direction.[53] As an alternative, other works assumed plane stress condition, which requires very thin tissue geometry undergoing in-plane loading only.[48] Neither of these requirements are met in the context of clinical breast USE. To assess the deviation of the plane strain and plane stress

assumptions from actual 3D situations, we conducted an *in-silico* experiment of breast USE using ABAQUS FE solver (ABAQUS 2019, Dassault Systèmes Simulia Corp., Johnston, Rhode Island, USA). In this experiment, a typical breast geometry derived from a breast MR image was converted into a homogeneous hyperelastic

breast FE model with hyperelastic parameters assigned based on values reported in the literature.[55] This model was virtually compressed by a US probe to simulate a typical USE procedure. The simulation was conducted using 3D geometry and loading as the ground truth model, while 2D plane strain and plane stress conditions

were also simulated to evaluate their deviation from the "true" 3D model. For this evaluation, the ratio of the mean difference between the "true" and 2D displacement fields to the mean value of the "true" field was calculated for both the axial and lateral displacement components. For the plane strain case, this led to values of 0.84 and 4.73 for the axial and lateral components, respectively. For the plane stress case, the ratio values were 0.79 and 2.87, respectively. While this experiment, which involves a single breast, is not rigorous, the obtained large values, especially the ones pertaining to the plane strain assumption are sufficient to motivate developing a modified incompressibility equation that can be used more reliably in breast USE.

In this study, we estimate the out-of-plane strain considering the breast undergoing a US probe loading as a semi-infinite medium. Stress resulting from a point load (P) applied to the surface of a semi-infinite medium at any point (T) in the medium can be estimated using the semi-infinite elastic model developed by Boussinesq (1885).[56] Axial and out-of-plane stresses can be calculated using Equations (7), (8), and (9). As shown in Figure 2, in these equations, (x_0, y_0, z_0) and (x, y, z) are the coordinates of point T and load P, respectively, while r is the Euclidean distance between them.

$$\sigma_{xx} = \frac{P}{2\pi} \left\{ \frac{3(y_0 - y)(x_0 - x)^2}{r^5} - (1 - 2\nu) \left[\frac{(x_0 - x)^2 - (z_0 - z)^2}{r\left(r^2 - (y_0 - y)^2\right)(r + (y_0 - y))} - \frac{(z_0 - z)^2(y_0 - y)}{r^3\left(r^2 - (y_0 - y)^2\right)} \right] \right\} \qquad (7)$$

$$\sigma_{yy} = \frac{3P}{2\pi} \frac{(y_0 - y)^3}{r^5} \qquad (8)$$

$$\sigma_{zz} = \frac{P}{2\pi} \left\{ \frac{3(y_0 - y)(z_0 - z)^2}{r^5} - (1 - 2\nu) \left[\frac{(z_0 - z)^2 - (x_0 - x)^2}{r\left(r^2 - (y_0 - y)^2\right)(r + (y_0 - y))} - \frac{(x_0 - x)^2(y_0 - y)}{r^3\left(r^2 - (y_0 - y)^2\right)} \right] \right\} \qquad (9)$$

Assuming a uniformly distributed loading applied by the US probe on the surface of the breast, axial and out-of-plane stresses at every point in the US FOV (Figure 3a) can be calculated by integration of Equations (7), (8), and (9) on the surface of the applied load. Thus, using Hooke's law, the axial and out-of-plane
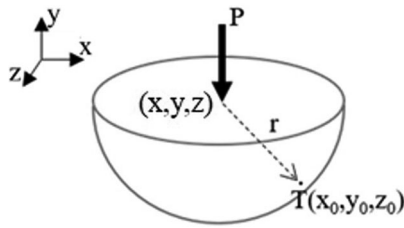
FIGURE 2 Boussinesq's model: a schematic of a semi-infinite medium under a point load

strains can be calculated as given in Equation (10) where μ and λ are Lame' parameters.

$$
\begin{bmatrix} \varepsilon_{yy} \\ \varepsilon_{zz} \end{bmatrix} = \begin{bmatrix} \dfrac{-\lambda}{2\mu(3\lambda+2\mu)} & \dfrac{\lambda+\mu}{\mu(3\lambda+2\mu)} & \dfrac{-\lambda}{2\mu(3\lambda+2\mu)} \\[2ex] \dfrac{-\lambda}{2\mu(3\lambda+2\mu)} & \dfrac{-\lambda}{2\mu(3\lambda+2\mu)} & \dfrac{\lambda+\mu}{\mu(3\lambda+2\mu)} \end{bmatrix}
$$
$$
\times \begin{bmatrix} \sigma_{xx} \\ \sigma_{yy} \\ \sigma_{zz} \end{bmatrix} \qquad (10)
$$

In this work, we assume that the breast is linear elastic with a Young's modulus, E, value of 3 kPa[63] and Poisson's ratio of 0.495. The Poisson's ratio value is consistent with the high-water or lipid content composition of most soft tissue, including breast tissue. While some intra- and inter-patient variability in these parameters is expected, our simulations have indicated that modest variability does not impact estimated displacement fields substantially. The Lame' parameters can be calculated using the following equation.[60]

$$
\lambda = \frac{E\nu}{(1+\nu)(1-2\nu)} \;,\; \mu = \frac{E}{2(1+\nu)} \qquad (11)
$$

Thereafter, the ratio ($k = \dfrac{\partial u_z}{\partial z} \Big/ \dfrac{\partial u_y}{\partial y} = \dfrac{\varepsilon_{zz}}{\varepsilon_{yy}}$) of the out-of-plane to axial strains can be calculated and incorporated in Equation (6), leading to the following modified incompressibility equation.

$$
\partial u_x/\partial x + (k+1)\,\partial u_y/\partial y = 0 \qquad (12)
$$

The finite difference form of this equations can be rewritten in a matrix form as follows:

$$
CU = 0 \qquad (13)
$$

Here, U contains the lateral and axial displacements only, and C is a matrix containing coefficients of the finite difference approximation of Equation (12), which depends on k values calculated for each point within the FOV. C is dependent on the dimensions of the FOV only and can be calculated offline and stored for use in efficient estimation of improved displacements. Having this equation in addition to the displacement fields obtained from the previous step (U_m is equal to U_{new} obtained from Equation (4) (i.e., $IU = U_m$)), we can form the following linear system of equations and solve it to obtain an improved estimate of U.

$$
\begin{bmatrix} C \\ I \end{bmatrix} U = \begin{bmatrix} 0 \\ U_m \end{bmatrix} \rightarrow AU = b \qquad (14)
$$

In this work, we seek $U \in \mathbb{R}$ which minimizes $\frac{1}{2}U^T A^T A U - (A^T b)^T U$. As such, Equation (14) can be solved efficiently using the Polak-Ribiere conjugate gradient method.[57] Since the initial estimate of axial displacements are known to be more accurate than their lateral counterparts, we also employed weighted least-squares optimization[58] in solving Equation (14). For this purpose, W was considered as the weight diagonal matrix where $w_{i,i}$ represents the importance of the ith row in Equation (14). This equation is an augmented system consisting of three different sets
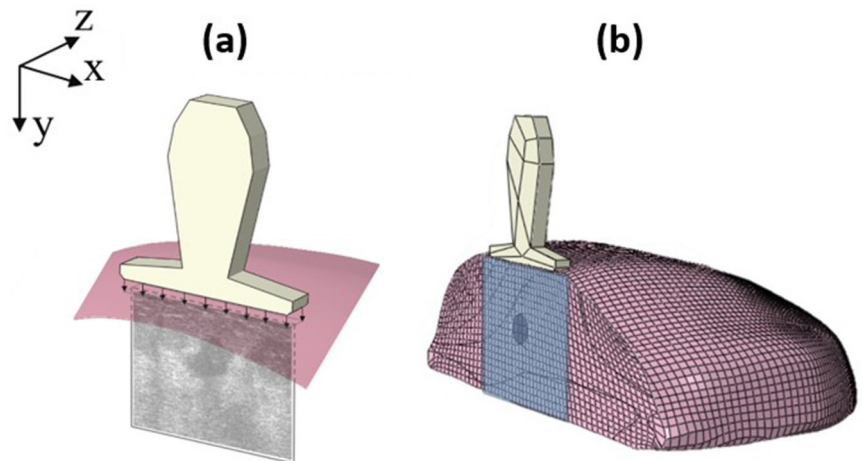
FIGURE 3 (a) Part of the breast surface under a rectangular contact pressure of the US probe and image's rectangular FOV where at each point of this FOV, the stress values are calculated by integration of Equations (7), (8), and (9) over the probe's contact surface. (b) Part of the breast FE model cut at the spherical tumor region with a rigid US probe pushing against the breast. The rectangular surface mimics the US FOV.

TABLE 1 Different weight sets used for enforcing tissue incompressibility

	WS1	WS2	WS3
Incompressibility Equation	1	5	10
Lateral Displacement	1	1	1
Axial Displacement	10	10	10

TABLE 2 Hyperelastic parameters (N/mm^2) of normal and tumor tissues used in the breast model

	C10	C01	C20	C11	C02
Normal	3.1e-4	3e-4	22.5e-4	38e-4	47.2e-4
Tumor	8.5e-4	8e-4	40e-4	60e-4	80e-4

of equations. With $m \times n$ data grid, the first part has $N_1 = (m-1) \times (n-1)$ rows which is related to incompressibility and the second and third parts each have $N_2 = m \times n$ rows pertaining to the measured axial and lateral displacements, respectively. For each part, we assign a single weight denoted by w_{inc}, w_{lat} and w_{ax} corresponding to the incompressibility, lateral displacements, and axial displacements, respectively, leading to the weight matrix given in Equation (15). With this alternative, we form $WAU = Wb$ and use the Polak-Ribiere conjugate gradient method to solve it, leading to a further refined displacement field.

$$W = \begin{bmatrix} w_{inc} & & & & & & \\ & w_{lat} & & & & & \\ & & w_{ax} & & 0 & & \\ & & & \ddots & & & \\ & 0 & & & w_{inc} & & \\ & & & & & w_{lat} & \\ & & & & & & w_{ax} \end{bmatrix}$$

(15)

In this work, we used the three different weight sets presented in Table 1. The rationale for choosing these weight factors is based on the reliability of each set of data. In these sets, the ratio of w_{ax} to w_{lat} was set to 10 based on a typical noise amplitude ratio of 10:1 between axial and lateral displacement data.[59] The w_{inc} was assigned three different values of 1, 5, and 10. These weight sets were evaluated using an *in-silico* phantom study as discussed in Section 2.2.1.

2.1.3 | Step 3: Strain Compatibility Enforcement

The final step in the proposed method is enforcing the tissue strain compatibility.[60] The equation governing strain compatibility is given below in terms of the strain tensor components:

$$\frac{\partial^2 \varepsilon_{xx}}{\partial y^2} + \frac{\partial^2 \varepsilon_{yy}}{\partial x^2} - 2\frac{\partial^2 \varepsilon_{xy}}{\partial x \partial y} = 0$$

(16)

Using the finite difference method, a numerical approximation of this equation was derived for each rectangular four-noded element formed in the computation grid. Through applying the equation to all elements in the computation grid of the FOV, the following matrix equation can be obtained:

$$P\varepsilon = 0$$

(17)

Here, ε is a vector containing lateral, axial and shear strains, and P is a coefficient matrix containing parameters of the finite difference approximation of the compatibility equation. Combined with the strains (ε_m) calculated based on the refined displacements obtained in the previous step, the following system of equations can be obtained.

$$\begin{bmatrix} P \\ I \end{bmatrix} \varepsilon = \begin{bmatrix} 0 \\ \varepsilon_m \end{bmatrix} \rightarrow B\varepsilon = e$$

(18)

This equation can be solved using the Polak-Ribiere method to obtain a further refined estimate of the strain.

2.2 | Methods Validation

2.2.1 | *In-Silico* Breast Phantom Study

The proposed method was first validated using an *in-silico* breast biomechanical model. To generate the breast *in-silico* model, a typical breast geometry was segmented from 3D US images using 3D Slicer (www.slicer.org). To generate the breast FE mesh, the segmented geometry was processed using IA-FEMESH (MIMX, Iowa city, Iowa, USA). A spherical inclusion was defined within the breast mesh to mimic a breast tumor. The FE mesh of the breast model consists of 58,294 eight-noded hexahedral hybrid elements type C3D8H and 63,519 nodes. For better realism, the breast tissue, including the background and tumor regions was modeled as hyperelastic material using the polynomial model. The hyperelastic parameters of the normal and tumor tissues in the breast model were assigned based on values given in Table 2 according to the literature.[55,61]

For simulating breast compression using a US probe mimicking a typical USE procedure, ABAQUS FE solver (ABAQUS 2019, Dassault Systèmes Simulia Corp., Johnston, Rhode Island, USA) was used. The probe's loading was applied using a contact mechanics model following the master-slave approach. To improve the simulation realism, the contact problem was carried out

in two steps. In the first step, the probe was lowered onto the breast model until it was in full contact with the surface of the breast. The second step involved further quasi-static compression to achieve the breast's desired deformation. After deforming the breast model, we obtained the displacement field within the mid-plane beneath the probe. As shown in Figure 3b, this mid-plane represents the US FOV. Consistent with USE, only the displacements pertaining to the second compression step was considered to mimic the displacement data. To add more realism to the displacement data obtained from this simulation, Gaussian noise was added such that the ratio of noise amplitude of the lateral to the axial directions was 10, leading to SNR values of 40 and 13.5 for the axial and lateral displacements, respectively. For validation, we input this simulated noisy displacement field to the developed algorithm and compared the output displacement field with the noise free version using the normalized cross correlation (NCC) given in Equation (19) as a similarity criterion. In this equation, X and Y represent the two images being compared, $\overline{x}$ and $\overline{y}$ are the mean values of their respective image intensity distribution, and σ_X^2 and σ_Y^2 are their variances. Utilizing the displacement field generated in this part, we evaluated and compared the validity of the incompressibility Equation (12) developed based on Boussinesq's model against the one developed using the plane strain model-based incompressibility Equation 6.

$$NCC\,(X,\,Y) = \frac{1}{N}\frac{\sum_{i=1}^{N}\left(x_i - \overline{x}\right) \cdot (y_i - \bar{y})}{\sqrt{\sigma_X^2 . \sigma_Y^2}} \qquad (19)$$

To determine a proper weight set of equations among the three candidates given in Table 1, we used an ad hoc method whereby the NCC value between the "true" and refined displacement fields and the number of grid elements that satisfy the compatibility equation accurately were evaluated. The best selected weight set candidate was the one that led to the highest NCC value and largest number of compatible elements.

2.2.2 | Tissue-mimicking Breast Phantom Study

To evaluate the displacement enhancement, the proposed method was applied to three separate tissue-mimicking breast phantoms consisting of soft background and stiff tumor tissues. The first phantom is Breast Elastography Phantom Model 059 (Computerized Imaging Reference Systems (CIRS; Pacific Northwest X-ray Inc., Gresham, USA). The size, shape, and ultrasonic characteristics of this phantom mimic that of an average human breast in supine position while

it contains several lesions ranging in size from 3 to 10 mm in diameter. Two different regions of the phantom, henceforth called Phantom A and B, were tested. The second phantom, referred to as Phantom C, is a block-shaped phantom with a single inclusion (CIRS; Pacific Northwest X-ray Inc., Gresham, USA). For data acquisition of the first and second phantoms, the US probe was controlled with a mechanical device to compress the phantom with 0.1 inches steps and the US RF data was acquired using an Antares Siemens system (Issaquah, Washington, USA) and a VF10-5 linear array transducer at a center and sampling frequencies of 6.67 and 40 MHz, respectively. The last phantom, D, was a breast-shaped phantom constructed in our laboratory using gelatin and agar dissolved in water.[62] The RF data for this phantom was acquired using an Ultrasonix RP system (Ultrasonix Medical Corporation, Richmond, British Columbia, Canada) and a L14-5/38 linear array transducer with a nominal frequency of 10 MHz at a sampling frequency of 20 MHz. The displacement and strain fields were initially estimated using the GLUE and SOUL methods. We then refined the displacement and strain fields using the proposed technique, STREAL. To assess quality improvement in the strain images, the following unitless metrics of signal to noise ratio (SNR) and contrast-to-noise ratio (CNR) were used:

$$SNR = \frac{\bar{s}}{\sigma} \qquad (20)$$

$$CNR = \sqrt{\frac{2\left(\overline{s_b} - \overline{s_t}\right)^2}{\sigma_b^2 + \sigma_t^2}} \qquad (21)$$

Here, $\bar{s}$ and σ are the spatial average and variance of a window in the strain image, respectively. Similarly, $\bar{s}_b$, $\bar{s}_t$, σ_b, and σ_t are the spatial average and variance of strains of a window in the target and background areas, respectively.

To further evaluate the performance of the STREAL method, the three-breast tissue-mimicking phantoms were simulated using ABAQUS FE solver (ABAQUS 2019, Dassault Systèmes Simulia Corp., Johnston, Rhode Island, USA). The geometries of these phantoms followed those of the actual phantoms A/B, C, and D, respectively. Spherical inclusions were placed inside the generated *in-silico* phantoms consistent with the actual phantoms' inclusions. The models were all linear elastic with the same Young's moduli as the actual phantoms. Quasi-static stimulations were then applied to the surfaces of the phantoms before the displacement fields of the mid-plane of the phantoms were computed. NCC was used to compare these fields to the estimated ones obtained from the GLUE, SOUL and STREAL methods.
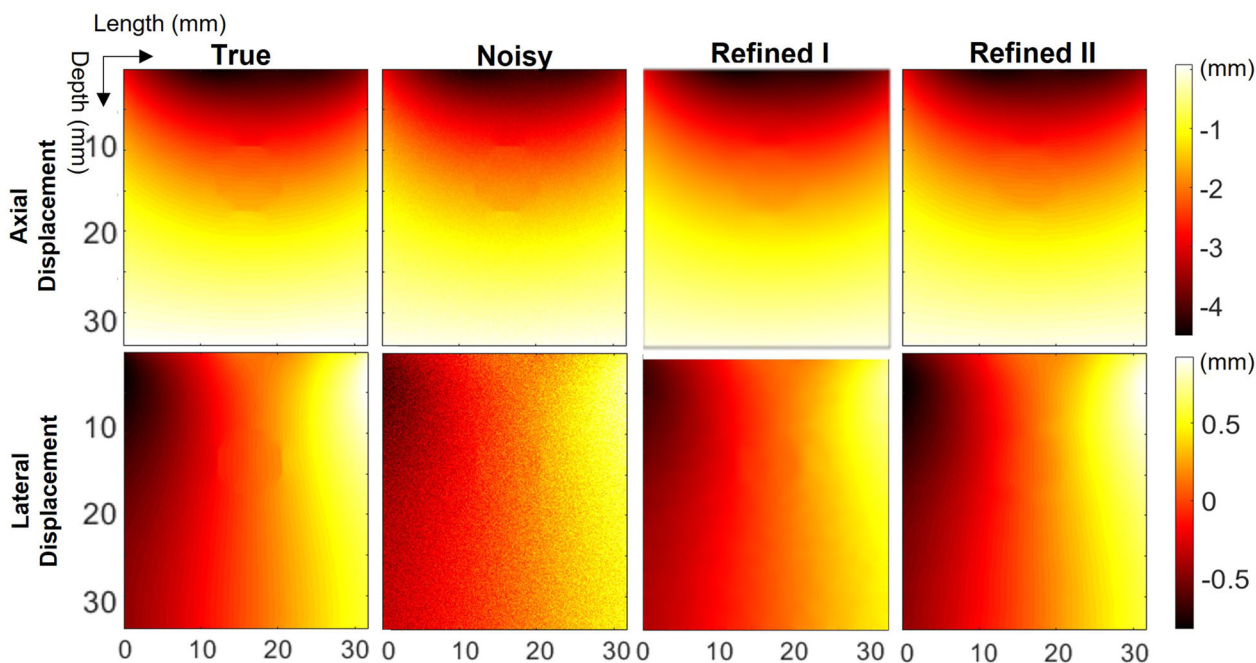
FIGURE 4 Original displacement fields generated from the *in-silico* breast model, their noisy counterparts, and refined displacement fields after steps 1 (Refined I) and 2 (Refined II) of STREAL

TABLE 3 NCC values of displacement and strain fields generated using the algorithm steps with corresponding "true" fields in the *in-silico* phantom study

NCC with ground truth (*in-silico*)		
Axial Displacement	Noisy	0.9333
	Refined I	0.9966
	Refined II	1.0000
Lateral Displacement	Noisy	0.8757
	Refined I	0.9666
	Refined II	0.9997
Axial Strain	Noisy	0.0764
	Refined I	0.5908
	Refined II	0.5965
	Refined III	0.6922
Lateral Strain	Noisy	0.0161
	Refined I	-0.1323
	Refined II	0.2066
	Refined III	0.2244

2.2.3 | Clinical Breast Ultrasound Elastography Case Study

Further evaluation of the proposed method was carried out using USE data acquired from two breast cancer patients in accordance with institutional research ethics approval. A Sonix RP System (Ultrasonix, Vancouver, Canada) and a L14-5/60 transducer with a nominal frequency of 10 MHz was used to acquire US B-mode images and RF data at a rate of 12 frames/s. The RF data were collected at pre- and post- compression states of a quasi-static stimulation of the breast using the US probe by a trained sonographer. Similar to the phantom study, initial displacements and strain fields were estimated using the GLUE and SOUL methods before they were refined using the STREAL algorithm. SNR and CNR of the strain images before and after using the STREAL algorithm were calculated for image quality comparison.

3 | RESULTS

3.1 | *In-Silico* Breast Phantom Study

The simulated axial and lateral displacement fields in the FOV plane of the *in-silico* breast phantom, including their noisy counterparts, are shown in Figure 4. This figure also illustrates the refined displacement fields using steps 1 and 2 of the proposed STREAL method. To show the progressive improvement achieved through each step of the algorithm, NCC values of images obtained with the noisy images and each of their refined counterpart are reported in Table 3.

Tissue incompressibility was calculated at each point within the FOV using the plane-strain assumption and the Boussinesq's derived model. This led to the images shown in the top row of Figure 5 where visual assessment shows that the incompressibility image of Figure 5b is closer to the ideal uniformly zero-value region compared to the image in Figure 5a which shows
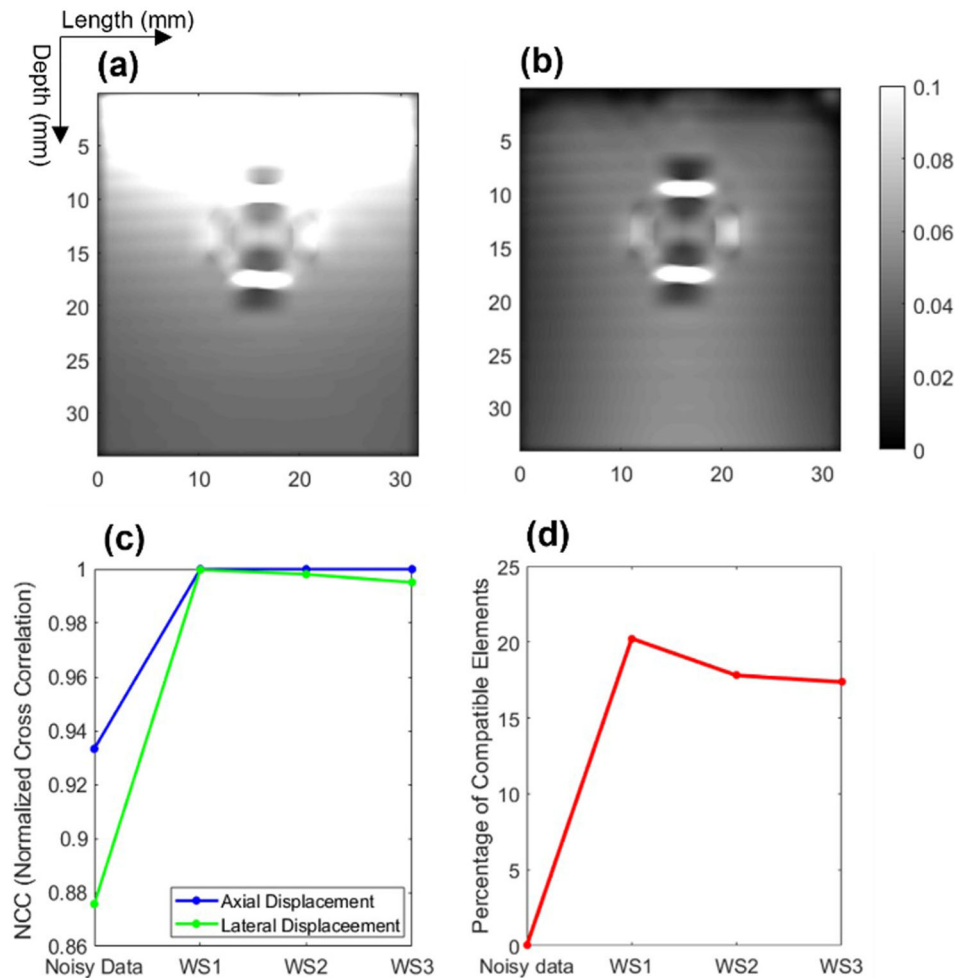
FIGURE 5 Tissue incompressibility images calculated based on (a) plane strain assumption and (b) semi-infinite medium model. The latter is closer to uniformly black image that represents an ideal incompressible tissue. (c) The NCC similarity measure between the "true" and refined displacements, (d) percentage of compatible elements based on a threshold value of 0.02 obtained by calculating the absolute value of a finite difference approximation of the compatibility Equation 16

large values of incompressibility at the top. Compared to the theoretical value of 0, the norms of these images are 32.83 and 14.75 for the plane-strain and Boussinesq's derived models, respectively. This indicates that the tissue incompressibility distribution obtained based on the proposed Boussinesq's derived model is superior to its plane-strain derived counterpart. Figure 5c illustrates the plot of NCC between the "true" and refined axial and lateral displacement fields against the weight set candidates given in Table 1. Figure 5d shows a plot of percentage of compatible elements in the computational grid meeting a compatibility threshold value of 0.02 obtained by calculating the absolute value of a finite difference approximation of the compatibility Equation 16. The plots indicate that the weight set WS1 leads to the best outcome. It also shows that the WS1 set leads to ~20% compatible elements, which may seem low; however, it should be noted that this percentage increases substantially by relaxing the compatibility threshold value such that near compatible elements are included.

Finally, Figure 6 illustrates the refined strain fields using steps 1, 2, and 3 of the proposed method. In this paper, both axial and lateral strain images follow a convention of positive and negative values for compressive and tensile strains, respectively. To demonstrate the progressive improvement achieved through each step of the algorithm, NCC values of images obtained with the noisy images and each of their refined counterpart are reported in Table 3.

3.2 | Tissue-mimicking Breast Phantom Study

Figure 7 illustrates the results generated for the four tissue-mimicking phantom cases, A, B, C, and D. It includes the axial and lateral displacement results generated by the GLUE, SOUL, proposed STREAL techniques in addition to displacement fields obtained by FE simulation which represents the ground truth.
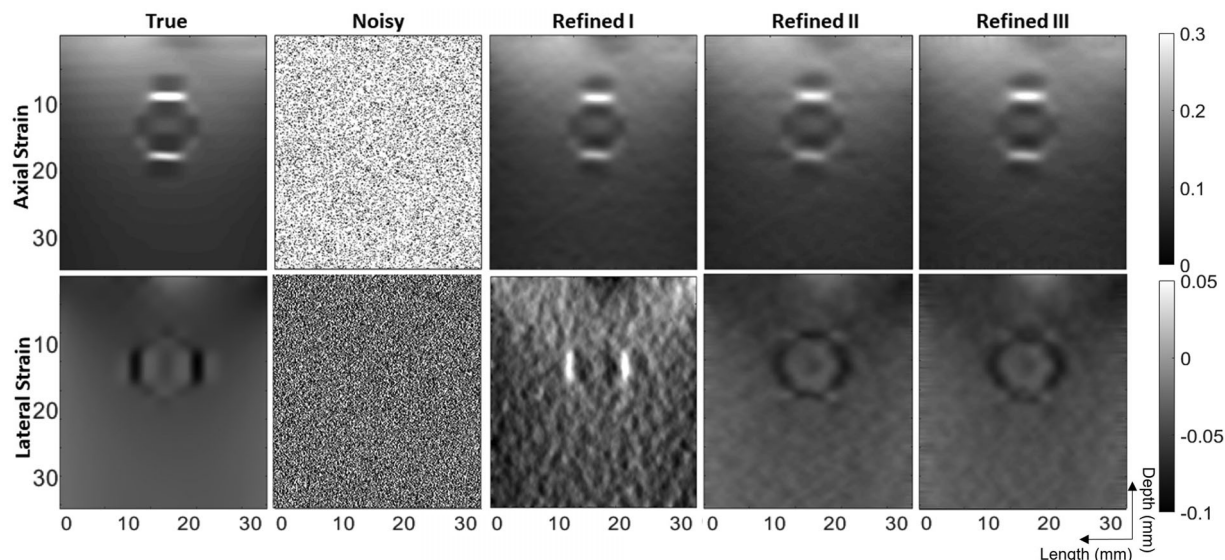
FIGURE 6 True and refined strain fields in the *in-silico* breast phantom after three stages (refinements) of applying STREAL. Compressive and tensile strains are considered positive and negative, respectively
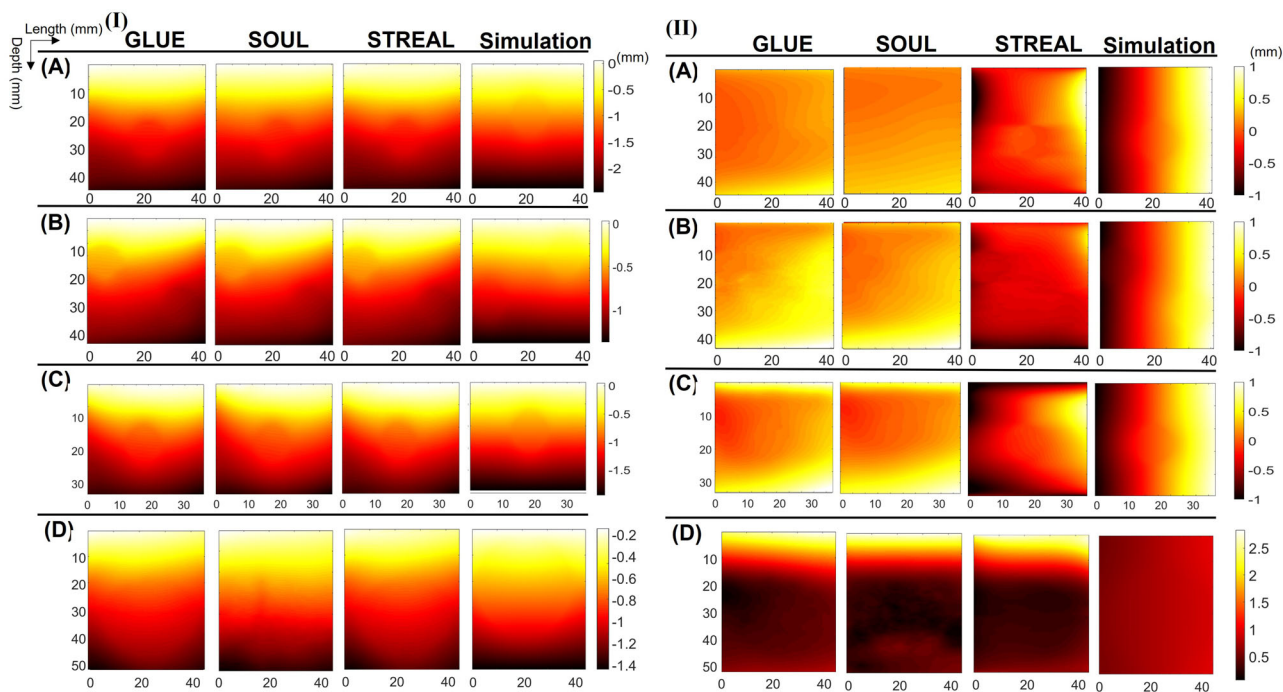
FIGURE 7 Axial (I) and lateral (II) displacement fields obtained from GLUE, SOUL, the proposed STREAL methods and FE simulation ("ground truth") for phantom cases A-D. Note that these results were obtained after performing the first two steps of the STREAL algorithm since the third step only applies to strain fields

Generally, this figure indicates that in contrast to the axial displacement fields that show some improvement, the lateral displacement fields obtained by the STREAL technique are improved substantially as the latter fields show clear evidence of the inclusions while they are closer to the "ground truth" results. This figure leads to very interesting observations concerning the lateral displacement maps. For example, in Phantoms A and B and C, the lateral displacement maps obtained by the STREAL method are the only ones that show the expected antisymmetric pattern w.r.t. the vertical center line while they contain features consistent with the single or double circular inclusions with the respective phantoms' true size and location. Moreover, consistent
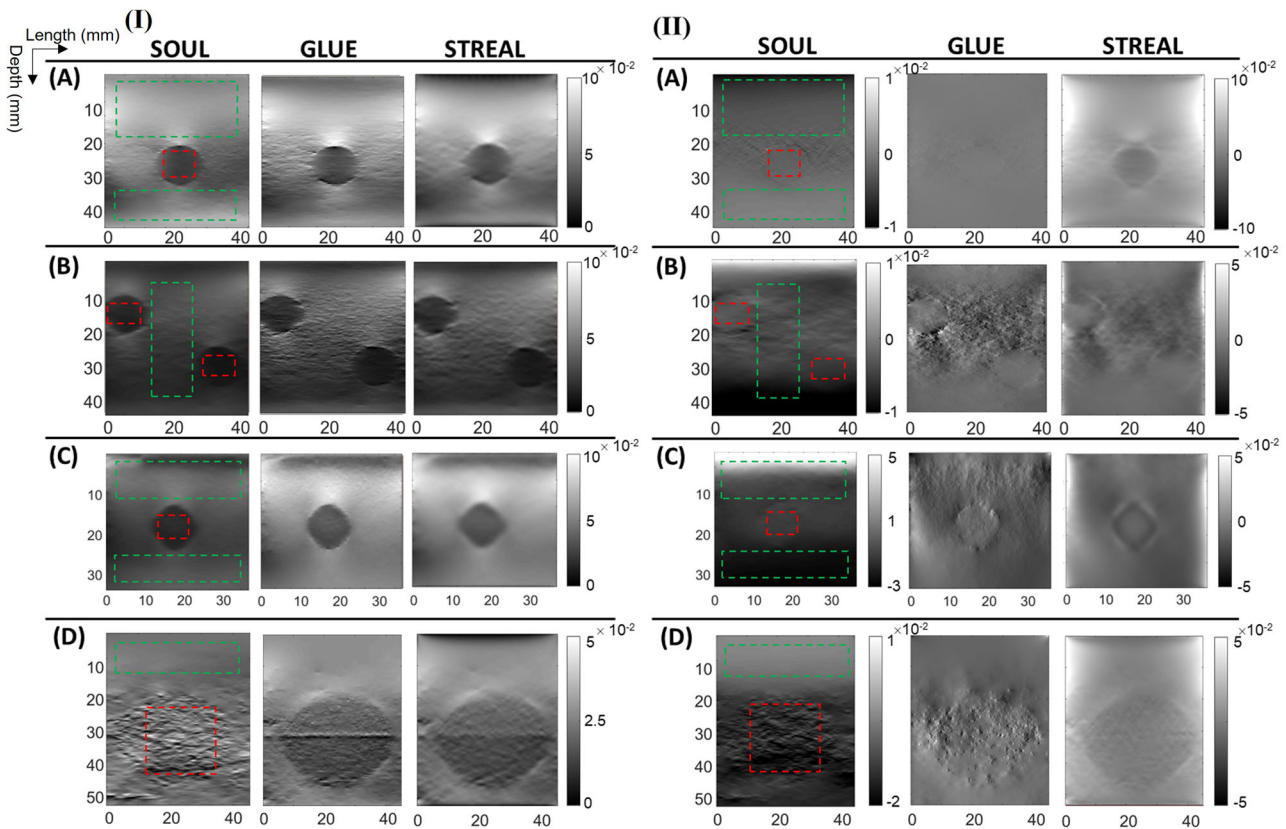
FIGURE 8 Axial (I) and lateral (II) strain images obtained from GLUE, SOUL, and the proposed STREAL method for phantom cases A-D. In this figure, positive and negative values represent compression and tensile strains, respectively. Due to inconsistency between the lateral strain values of different methods, different color bars are adjusted for each method to have the best visualization. Background and target areas used to calculate the SNR and CNR values are also outlined using dashed lines as they appear in the first columns of the two sets of images

with the large circular inclusion in Phantom D, among produced lateral displacement maps, the one generated by the STREAL method shows clearer features pertaining to presence of a large circular inclusion located in the middle. These observations are indicative of the accuracy of the STREAL method in producing accurate lateral displacement maps. Figure 8 illustrates the phantom strain images obtained using the GLUE, SOUL, and proposed STREAL techniques. This figure shows that the proposed method is capable of generating substantially better-quality axial strain and superior quality lateral strain compared to both the GLUE and SOUL methods. Generally, axial strain images generated by the STREAL method are less noisy while they include less artifacts compared to the ones produced by the other two methods. As for the lateral strains, judged by the quality of the known phantoms' geometry characteristics produced by the STREAL method compared to the other methods, it can be concluded once again that the quality of the lateral strain maps obtained by the STREAL method is more favorable.

The calculated SNR and CNRs based on background and target areas of the tissue-mimicking phantoms shown in Figure 8 are presented in Table 4. On average,

this table shows that the STREAL technique is successful in improving the SNR and CNR of axial strain images of the phantoms by 44% and 63%, respectively, compared to the GLUE and SOUL techniques. The results also show that the STREAL technique is even more effective with lateral strain images of the phantoms with 130% and 435% improvement in the SNR and CNR, respectively. Table 5 shows the similarity between the displacement fields generated through the *in-silico* simulation of the phantoms and corresponding fields computed using the GLUE, SOUL, and STREAL methods. It also shows the range of percentage improvements of the similarity values obtained using the STREAL method over corresponding values obtained from the GLUE and SOUL methods at 7−84% and 26−140% for axial and lateral displacement images, respectively. Once again, these results indicate that while compared to the GLUE and SOUL methods, the STREAL method leads to some improvement in the accuracy of axial displacements, it leads to highly favorable quality lateral displacements. Overall, the phantoms show a high level of improvement in their displacement fields, while an exception is Phantom D which shows the least amount of improvement. This is anticipated as the thickness of the breast

TABLE 4 Calculated SNR and CNR metrics for axial and lateral strain images of the four phantoms

Phantom	Image	SNR			CNR		
		GLUE	SOUL	STREAL	GLUE	SOUL	STREAL
A	Axial Strain	8.7	15.9	18.8	5	5.2	10.4
	Lateral Strain	2.7	2.5	13.2	0.8	0.8	12.3
B	Axial Strain	3.9	4.2	7.1	1.1	1	2.1
	Lateral Strain	1.7	2.1	3.2	1.4	1.2	1.9
C	Axial Strain	9.1	8.9	9.1	4.5	3.2	4.6
	Lateral Strain	2.2	1.6	2.6	1	0.8	3.3
D	Axial Strain	8.5	9.3	11.6	3.6	2.4	3.6
	Lateral Strain	3.3	4.2	3.7	0.8	1.2	0.8
Improvement for Phantoms	Axial Strain	59 ± 44%	29 ± 25%		50 ± 49%	76 ± 29%	
	Lateral Strain	127 ± 154%	133 ± 173%		426 ± 591	444 ± 28	
Clinical Cases 1	Axial Strain	1.63	1.63	2.39	1.70	1.72	3.42
	Lateral Strain	1.08	1.11	1.53	0.16	0.16	0.22
Clinical Case 2	Axial Strain	1.21	1.21	3.29	1.12	1.12	4.81
	Lateral Strain	0.83	2.14	2.95	0.42	3.33	3.96

TABLE 5 Similarity between displacement fields generated by the *in-silico* simulation of the tissue mimicking phantoms and corresponding fields computed by the GLUE, SOUL, and STREAL methods

Phantom	Image	NCC with the generated counterpart using *in-silico* simulation		
		GLUE	SOUL	STREAL
A	Axial Displacement	0.9917	0.9919	0.9925
	Lateral Displacement	0.5907	0.3695	0.8881
B	Axial Displacement	0.921	0.92	0.9213
	Lateral Displacement	0.4302	0.5183	0.7909
C	Axial Displacement	0.8887	0.8384	0.8894
	Lateral Displacement	0.4944	0.3795	0.6601
D	Axial Displacement	0.9531	0.8919	0.9643
	Lateral Displacement	0.4909	0.4138	0.5234
Improvement for Phantoms	Axial Displacement	0.3 ± 0.5%	4 ± 3%	
	Lateral Displacement	44 ± 28%	73 ± 42%	

phantom D was very limited, hence the semi-infinite medium model was not effective. Such a small thickness is less likely to be encountered in typical breasts, hence the proposed method is generally expected to offer substantial improvement in clinical applications.

3.3 | Clinical Breast Ultrasound Elastography Case Study

Figure 9 shows breast B-mode images of the two clinical cases. The axial and lateral strain images generated by the GLUE, SOUL and STREAL methods for these clinical cases are shown in Figure 10. Visual assessment of this figure indicates that the axial and lateral strain images generated by the STREAL method compared to the other methods are generally less noisy while their background regions are more uniform. Furthermore, in Case 2 where the tumor is centered within the FOV, unlike GLUE and SOUL, STREAL shows that the lateral strain is predominantly tensile. The latter observation is more consistent with what is expected according to Poisson effect. Quantitative assessment of the data pertaining to the clinical cases based on the bottom rows of Table 4 demonstrate that STREAL leads to substantial improvement in the SNR and CNR of both the axial and lateral strain estimates compared to GLUE and SOUL.

4 | DISCUSSION

In this work, we presented a novel method for computing tissue displacement and strain fields generated in typical
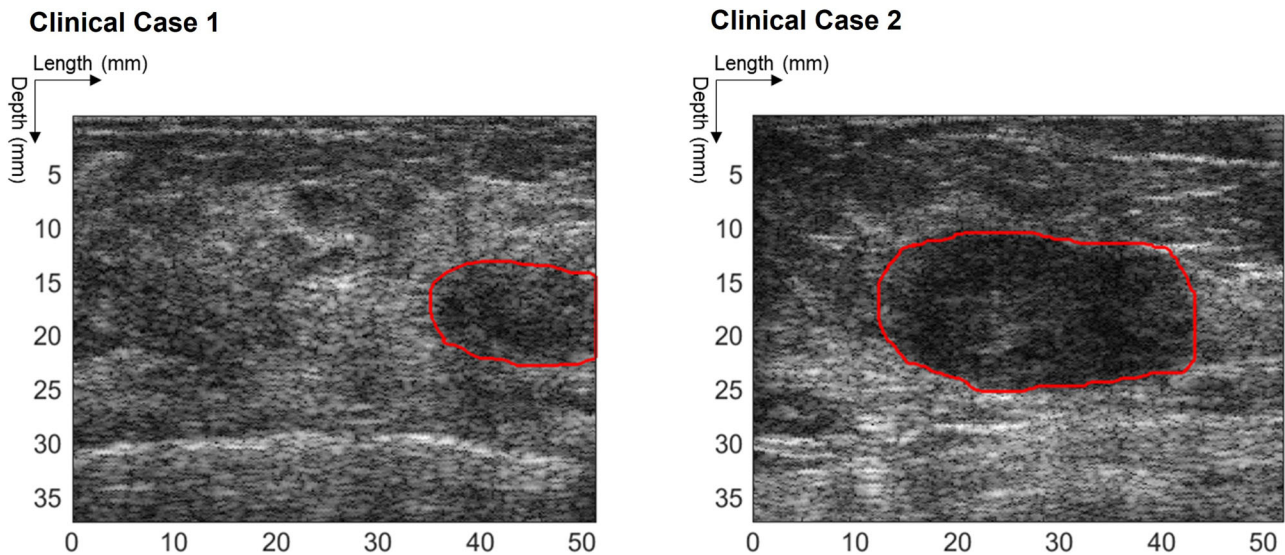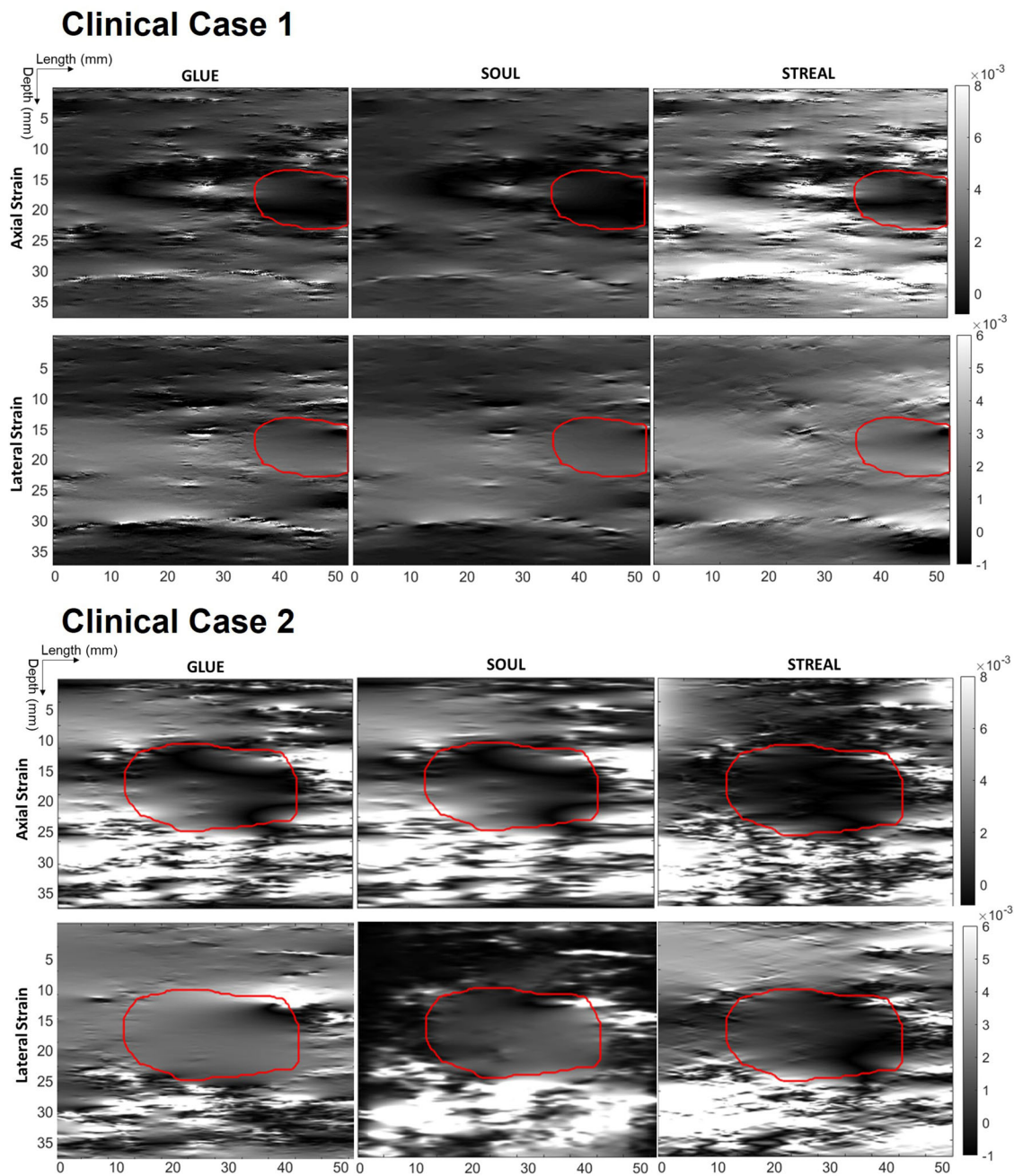
FIGURE 9 B-mode images of two clinical cases where the red outlines show tumor areas

US imaging. The method was designed for applications in quasi-static USE, including breast, prostate, and liver elastography. In addition to enhancement of axial displacement images where the field has already made substantial progress, a major feature of the proposed method is its ability to obtain accurate lateral displacement and strain images. The proposed method attempts to take full advantage of available constraints governing the tissue mechanics. In addition to enforcing displacement field continuity conditions, this technique utilizes tissue biomechanics principles for further improvement of strain image accuracy. The principles include tissue incompressibility and deformation compatibility which are incorporated in the model to generate accurate estimations of both axial and lateral displacement and strain images. To enforce tissue incompressibility, we developed a method which utilizes the Boussinesq semi-infinite analytical model to estimate the out-of-plane strain component before its incorporation in the general tissue incompressibility equation. To our knowledge, we are the first group to consider an estimate of the out-of-plane strain in tissue 2D motion tracking pertaining to USE. After enforcing tissue incompressibility, the proposed technique enforces the fundamental deformation compatibility equation to further enhance the strain field. While other investigators have utilized this equation to assess the quality of estimated displacement fields,[52] to our knowledge, the STREAL algorithm is the first to incorporate the compatibility equation for strain field refinement. Unlike other methods where continuity based regularization is imposed at the RF data processing stage,[33,34,40,41,44] the proposed technique is formulated to improve previously estimated displacement and strain images irrespective of their source and imaging modality. While we used initial displacement fields generated using the GLUE

technique in this work, using less regularized fields also led to highly accurate results.

In breast USE, the breast can be idealized as a semi-infinite medium and out-of-plane strain can be analytically calculated using the Boussinesq model. We first used this idealization with synthetic displacement data obtained from a simulated breast after it was contaminated with realistic noise. The results shown in Figure 4 indicates that the method is successful in almost entirely eliminating the noise of the displacement fields while Figure 6 shows very good ability to recover both of the axial and lateral strain images after highly exaggerated contamination with noise. Furthermore, Table 3 shows increasing similarity between the "ground truth" displacement and strain images and their image counterparts obtained through the successive steps of the proposed method. The increase of similarity for the lateral displacement and strain images is more remarkable. The *in-silico* breast model represents a reasonable breast model in terms of geometry and material behavior. Hence, the semi-infinite model used to develop the incompressibility equation in this work is anticipated to be effective with clinical data as long as the breast is large enough and the probe position is far from the breast's peripheral region. The presented formulation involves weight factors pertaining to axial and lateral data in addition to tissue incompressibility. In this investigation, we attempted to find the optimal set of these factors, however, further investigation and more rigorous methods are required to find a robust set that can be reliably used in the clinic.

The proposed method was further validated using tissue-mimicking phantoms, including breast-shaped and block-shaped phantoms, with one or several inclusions. Figures 7 and 8 indicate that, in all phantom cases, the proposed method produces substantially

FIGURE 10 Axial and lateral strain images of the two clinical cases generated using the GLUE, SOUL, and STREAL techniques. The red outlines show the tumor areas based on the B-mode image

better and superior strain images compared to the GLUE and SOUL techniques for the axial and lateral directions, respectively. For example, in Figure 8, while the axial strain images obtained by the STREAL technique show only subtle improvement compared to images obtained by the GLUE and SOUL techniques, the lateral strain images obtained by show clear improvement judged by their symmetry in the symmetric phantoms A, C and D. Furthermore, for the tissue mimicking phantoms, Table 5 shows higher similarity between the "ground truth" displacement images and their image counterparts obtained through the proposed method compared

to those obtained with the GLUE and SOUL methods. The increase of similarity for the lateral displacement images is more remarkable. Results of the clinical cases shown Figure 10 indicate that the STREAL technique can improve axial and lateral strains as, compared to the images produced using the GLUE and SOUL methods, the background region is more uniform while the tumor area is more distinguishable. Compared to the phantom cases, the visual improvement in the clinical cases is less clear. This can be attributed to two factors. One is the more complex stiffness distribution in the clinical cases where muscle, ligament and

blood vessel regions exist, and the other is the general weakness of strain imaging in capturing tissue stiffness distribution with complex tissue geometry and stiffness distribution situations. Therefore, it is anticipated that using the improved strain images obtained from the STEAL method within full inversion based elastography framework can lead to better visualization.[62] The tissue-mimicking study results also indicate that the proposed method produces higher quality strain images compared to the GLUE and SOUL techniques as, according to Table 4, there is lateral strain SNR improvement of $127 \pm 154\%$ and $133 \pm 173\%$ and CNR lateral strain improvement of 426 ± 591 and 444 ± 28 over the GLUE and SOUL methods, respectively. It is also noteworthy that although the lateral strain images generated using the STREAL technique are substantially dissimilar to the ones generated using the GLUE and SOUL methods, the STREAL technique is substantially more successful in generating lateral strain images that capture mechanically plausible patterns consistent with the phantoms' geometry and stiffness distribution. For example, Figure 7 shows clear antisymmetric displacement patterns w.r.t the vertical centerline of the phantoms while showing clear characteristics consistent with the shape and size of the inclusions. Moreover, Figure 8 shows that lateral strain images generated by the STREAL method is the only one among others that exhibit high consistency with the phantoms' geometry and stiffness characteristics. This conclusion is supported by the measured displacement image similarity with corresponding ground truth images which indicates lateral displacement estimation accuracy improvement of $44 \pm 28\%$ and $73 \pm 42\%$ compared to the GLUE and SOUL, respectively. The improvement in the strain fields generated by STREAL is less obvious in the clinical cases. This can be attributed to the natural heterogeneity of both of the background and tumor tissues, US probe location on the breast and inherent limitations of strain imaging. Nevertheless, the clinical cases indicate similar trend in capturing main features of the breast tissue mechanics. For example, in Case 2 where the tumor is centered within the FOV, consistent with the Poisson effect, the lateral strain in the tumor area is predominantly tensile in contrast to corresponding strains generated by GLUE and SOUL where the corresponding strain is predominantly compressive. Therefore, while the GLUE and SOUL methods are capable of producing reasonably accurate axial strain images, the quality of their lateral strain images are generally low. In contrast, the proposed method is very promising in producing accurate lateral strain images. This can have a tangible impact in improving Young's modulus images generated using inversion techniques as the image reconstruction is generally known to involve an ill-posed inverse problem, hence it can benefit substantially from availability of additional high quality data.[62] Such measured data enrichment can potentially facilitate the development of more sophisticated elastography techniques targeting reconstruction of more realistic model (e.g. anisotropic tissue model) parameters.

Figure 5 indicates that using the Boussinesq model to enforce tissue incompressibility demonstrated substantial improvement in estimating displacement and strain over using simple models such as the plane strain. However, depending on the breast geometry, including its size, tumor size and location within the breast, and the location of the US probe w.r.t breast, the improved accuracy provided by Boussinesq model may decrease. More improved accuracy may be achieved by considering more realistic breast geometry and improved models to estimate the out-of-plane strain distribution before incorporation in the fundamental incompressibility constraint. A notable limitation of the proposed method is its foundation on linear elasticity which assumes small tissue deformation. This implies that it cannot be used for elastography techniques aimed at reconstructing tissue hyperelastic parameters.

5 | CONCLUSION

Based on the validation carried out in this investigation, which included various breast phantom USE cases and two clinical breast USE cases, the proposed method appears to be very effective in producing improved estimate of tissue displacement and strain images. Compared to improvement of the axial displacement and strain components, the improvement is highly remarkable for the lateral component. While the method shows promise for clinical applications, further investigation with several clinical cases is necessary for rigorous assessment of the method's performance in the clinic.

ACKNOWLEDGMENTS

CONFLICT OF INTEREST
The authors have no conflicts to disclose.

REFERENCES
1. Breast Cancer Statistics | How Common Is Breast Cancer?" Accessed February 25, 2022. https://www.cancer.org/cancer/breast-cancer/about/how-common-is-breast-cancer.html
2. Ghoncheh M, Pournamdar Z, Salehiniya H. Incidence and mortality and epidemiology of breast cancer in the world. *Asian Pacific J Cancer Prev*. 2016;17(S3):43-46. https://doi.org/10.7314/APJCP.2016.17.S3.43

3. Hoerger TJ, Ekwueme DU, Miller JW, et al. Estimated effects of the national breast and cervical cancer early detection program on breast cancer mortality. *Am J Prev Med*. 2011;40(4):397-404. https://doi.org/10.1016/j.amepre.2010.12.017

4. Stout NK, Lee SJ, Schechter CB, et al. Benefits, harms, and costs for breast cancer screening after US implementation of digital mammography. *J Natl Cancer Inst*. 2014;106(6). https://doi.org/10.1093/jnci/dju092

5. Von Euler-Chelpin M, Lillholm M, Vejborg I, Nielsen M, Lynge E. Sensitivity of screening mammography by density and texture: A cohort study from a population-based screening program in Denmark. *Breast Cancer Res*. 2019;21(1):111. https://doi.org/10.1186/s13058-019-1203-3

6. Ophir J. Elastography: A quantitative method for imaging the elasticity of biological tissues. *Ultrason Imaging*. 1991;13(2):111-134. https://doi.org/10.1016/0161-7346(91)90079-w

7. Ophir J, Alam SK, Garra B, et al. Elastography: Ultrasonic estimation and imaging of the elastic properties of tissues. *Proc Inst Mech Eng Part H J Eng Med*. 1999;213(3):203-233. https://doi.org/10.1243/0954411991534933

8. Sarvazyan AJ, Hall TW, Urban M, Fatemi MR, Aglyamov SS, Garra B. An overview of elastography-an emerging branch of medical imaging. *Curr Med Imaging Rev*. 2011;7(4):255-282. https://doi.org/10.2174/157340511798038684

9. Ondeck MG, Kumar A, Placone JK, et al. Dynamically stiffened matrix promotes malignant transformation of mammary epithelial cells via collective mechanical signaling. *Proc Natl Acad Sci U S A*. 2019;116(9):3502-3507. https://doi.org/10.1073/pnas.1814204116

10. Acerbi I, Cassereau L, Dean I, et al. Human breast cancer invasion and aggression correlates with ECM stiffening and immune cell infiltration. *Integr Biol (United Kingdom)*. 2015;7(10):1120-1134. https://doi.org/10.1039/c5ib00040h

11. Wei SC, Fattet L, Tsai JH, et al. Matrix stiffness drives epithelial-mesenchymal transition and tumour metastasis through a TWIST1-G3BP2 mechanotransduction pathway. *Nat Cell Biol*. 2015;17(5):678-688. https://doi.org/10.1038/ncb3157

12. Boyd NF, Li Q, Melnichouk O, et al. Evidence that breast tissue stiffness is associated with risk of breast cancer. *PLoS One*. 2014;9(7):e100937. https://doi.org/10.1371/journal.pone.0100937

13. Karimi H, Fenster A, Samani A. A novel fast full inversion based breast ultrasound elastography technique. *Phys Med Biol*. 2013;58(7):2219-2233. https://doi.org/10.1088/0031-9155/58/7/2219

14. Andrade WP, Lima ENP, Osório CABT, et al. Can FDG-PET/CT predict early response to neoadjuvant chemotherapy in breast cancer? *Eur J Surg Oncol*. 2013;39(12):1358-1363. https://doi.org/10.1016/j.ejso.2013.08.025

15. Correas JM, Tissier AM, Khairoune A, Khoury G, Eiss D, Hélénon O. Ultrasound elastography of the prostate: state of the art. *Diagn Interv Imaging*. 2013;94(5):551-560. https://doi.org/10.1016/j.diii.2013.01.017

16. Gherlan GS. Liver ultrasound elastography: more than staging the disease. *World J Hepatol*. 2015;7(12):1595-1600. https://doi.org/10.4254/wjh.v7.i12.1595

17. Gitau SN, Menge IK. Elastography in chronic liver diseases. In: *Ultrasound Elastography*. IntechOpen; 2020. https://doi.org/10.5772/intechopen.88228

18. Bharat S, Techavipoo U, Kiss MZ, Liu W, Varghese T. Monitoring stiffness changes in lesions after radiofrequency ablation at different temperatures and durations of ablation. *Ultrasound Med Biol*. 2005;31(3):415-422. https://doi.org/10.1016/j.ultrasmedbio.2004.12.020

19. Lubinski MA, Emelianov SY, O'Donnell M. Speckle tracking methods for ultrasonic elasticity imaging using short-time correlation. *IEEE Trans Ultrason Ferroelectr Freq Control*. 1999;46(1):82-96. https://doi.org/10.1109/58.741427

20. Skovoroda AR, Emelianov SY, Lubinski MA, et al. Theoretical analysis and verification of ultrasound displacement and strain imaging. *IEEE Trans Ultrason Ferroelectr Freq Control*. 1994;41(3):302-313. https://doi.org/10.1109/58.285463

21. Varghese T. Quasi-Static Ultrasound Elastography. *Ultrasound Clin*. 2009;4(3):323-338. https://doi.org/10.1016/j.cult.2009.10.009

22. Falou O, Sadeghi-Naini A, Prematilake S, et al. Evaluation of neoadjuvant chemotherapy response in women with locally advanced breast cancer using ultrasound elastography. *Transl Oncol*. 2013;6(1):17-24. https://doi.org/10.1593/tlo.12412

23. Pan X, Gao J, Tao S, et al. A two-step optical flow method for strain estimation in elastography: simulation and phantom study. *Ultrasonics*. 2014;54(4):990-996. https://doi.org/10.1016/j.ultras.2013.11.010

24. Pellot-Barakat C, Frouin F, Insana MF, Herment A. Ultrasound elastography based on multiscale estimations of regularized displacement fields. *IEEE Trans Med Imaging*. 2004;23(2):153-163. https://doi.org/10.1109/TMI.2003.822825

25. Behar V, Adam D, Lysyansky P, Friedman Z. Improving motion estimation by accounting for local image distortion. *Ultrasonics*. 2004;43(1):57-65. https://doi.org/10.1016/j.ultras.2004.02.022

26. Zakaria T, Qin Z, Maurice RL. Optical-flow-based b-mode elastography: application in the hypertensive rat carotid. *IEEE Trans Med Imaging*. 2010;29(2):570-578. https://doi.org/10.1109/TMI.2009.2038694

27. Zhou Y, Zheng YP. A motion estimation refinement framework for real-time tissue axial strain estimation with freehand ultrasound. *IEEE Trans Ultrason Ferroelectr Freq Control*. 2010;57(9):1943-1951. https://doi.org/10.1109/TUFFC.2010.1642

28. Tehrani AKZ, Rivaz H. Displacement estimation in ultrasound elastography using pyramidal convolutional neural network. *IEEE Trans Ultrason Ferroelectr Freq Control*. 2020;67(12):2629-2639. https://doi.org/10.1109/TUFFC.2020.2973047

29. Gao Z, Wu S, Liu Z, et al. Learning the implicit strain reconstruction in ultrasound elastography using privileged information. *Med Image Anal*. 2019;58:101534. https://doi.org/10.1016/j.media.2019.101534

30. Kibria MG, Rivaz H. GLUENet: Ultrasound elastography using convolutional neural network. *Lect Notes Comput Sci (including Subser Lect Notes Artif Intell Lect Notes Bioinformatics)*. 2018;11042 LNCS:21-28. https://doi.org/10.1007/978-3-030-01045-4_3

31. Rivaz H, Boctor EM, Choti MA, Hager GD. Real-time regularized ultrasound elastography. *IEEE Trans Med Imaging*. 2011;30(4):928-945. https://doi.org/10.1109/TMI.2010.2091966

32. Hashemi HS, Rivaz H. Global time-delay estimation in ultrasound elastography. *IEEE Trans Ultrason Ferroelectr Freq Control*. 2017;64(10):1625-1636. https://doi.org/10.1109/TUFFC.2017.2717933

33. Mirzaei M, Asif A, Rivaz H. Combining total variation regularization with window-based time delay estimation in ultrasound elastography. *IEEE Trans Med Imaging*. 2019;38(12):2744-2754. https://doi.org/10.1109/TMI.2019.2913194

34. Ashikuzzaman M, Gauthier CJ, Rivaz H. Global ultrasound elastography in spatial and temporal domains. *IEEE Trans Ultrason Ferroelectr Freq Control*. 2019;66(5):876-887. https://doi.org/10.1109/TUFFC.2019.2903311

35. Céspedes I, Ophir J, Insana M. Theoretical bounds on strain estimation in elastography. *IEEE Trans Ultrason Ferroelectr Freq Control*. 1995;42(5):969-971. https://doi.org/10.1109/58.464850

36. Walker WF, Trahey GE. A fundamental limit on delay estimation using partially correlated speckle signals. *IEEE Trans Ultrason Ferroelectr Freq Control*. 1995;42(2):301-308. https://doi.org/10.1109/58.365243

37. Zhu Y, Hall TJ. A modified block matching method for real-time freehand strain imaging. *Ultrason Imaging*. 2002;24(3):161-176. https://doi.org/10.1177/016173460202400303

38. Ashikuzzaman M, Sadeghi-Naini A, Samani A, Rivaz H. Combining first- and second-order continuity constraints in ultrasound elastography. *IEEE Trans Ultrason Ferroelectr Freq Control*. 2021;68(7):2407-2418. https://doi.org/10.1109/TUFFC.2021.3065884

39. Rivaz H, Boctor EM, Choti MA, Hager GD. Ultrasound elastography using multiple images. *Med Image Anal*. 2014;18(2):314-329. https://doi.org/10.1016/j.media.2013.11.002

40. Kuzmin A, Zakrzewski AM, Anthony BW, Lempitsky V. Multi-frame elastography using a handheld force-controlled ultrasound probe. *IEEE Trans Ultrason Ferroelectr Freq Control*. 2015;62(8):1486-1500. https://doi.org/10.1109/TUFFC.2015.007133

41. Basarab A, Lyshchik A, Delachartre P. Multi-frame motion estimation for freehand elastography and its application to thyroid tumor imaging. In: *2008 5th IEEE International Symposium on Biomedical Imaging: From Nano to Macro, Proceedings, ISBI*. 2008:532-535. https://doi.org/10.1109/ISBI.2008.4541050

42. Mirzaei M, Asif A, Fortin M, Rivaz H. 3D normalized cross-correlation for estimation of the displacement field in ultrasound elastography. *Ultrasonics*. 2020;102:106053. https://doi.org/10.1016/j.ultras.2019.106053

43. Wang Y, Bayer M, Jiang J, Hall TJ. An improved region-growing motion tracking method using more prior information for 3-D ultrasound elastography. *IEEE Trans Ultrason Ferroelectr Freq Control*. 2020;67(3):580-597. https://doi.org/10.1109/TUFFC.2019.2948984

44. Wang Y, Jiang J, Hall TJ. A 3-D region-growing motion-tracking method for ultrasound elasticity imaging. *Ultrasound Med Biol*. 2018;44(8):1638-1653. https://doi.org/10.1016/j.ultrasmedbio.2018.04.011

45. Chen L, Treece GM, Lindop JE, Gee AH, Prager RW. A quality-guided displacement tracking algorithm for ultrasonic elasticity imaging. *Med Image Anal*. 2009;13(2):286-296. https://doi.org/10.1016/j.media.2008.10.007

46. Jiang J, Hall TJ. A fast hybrid algorithm combining regularized motion tracking and predictive search for reducing the occurrence of large displacement errors. *IEEE Trans Ultrason Ferroelectr Freq Control*. 2011;58(4):730-736. https://doi.org/10.1109/TUFFC.2011.1865

47. Chen L, Housden RJ, Treece GM, Gee AH, Prager RW. A hybrid displacement estimation method for ultrasonic elasticity imaging. *IEEE Trans Ultrason Ferroelectr Freq Control*. 2010;57(4):866-882. https://doi.org/10.1109/TUFFC.2010.1491

48. Lubinski MA. Lateral displacement estimation using tissue incompressibility. *IEEE Trans Ultrason Ferroelectr Freq Control*. 1996;43(2):247-256. https://doi.org/10.1109/58.485950

49. Skovoroda AR, Lubinski MA, Emelianov SY, O'Donnell M. Nonlinear estimation of the lateral displacement using tissue incompressibility. *IEEE Trans Ultrason Ferroelectr Freq Control*. 1998;45(2):491-503. https://doi.org/10.1109/58.660158

50. Li H, Porée J, Chayer B, Cardinal MHR, Cloutier G. Parameterized strain estimation for vascular ultrasound elastography with sparse representation. *IEEE Trans Med Imaging*. 2020;39(12):3788-3800. https://doi.org/10.1109/TMI.2020.3005017

51. O'Donnell M, Chen X, Kaluzynski K, Emelianov SY, Skovoroda AR. Strain magnitude estimation based on adaptive incompressibility processing. *Proc IEEE Ultrason Symp*. 2001;2:1643-1646. https://doi.org/10.1109/ULTSYM.2001.992037

52. Babaniyi OA, Oberai AA, Barbone PE. Recovering vector displacement estimates in quasistatic elastography using sparse relaxation of the momentum equation. *Inverse Probl Sci Eng*. 2017;25(3):326-362. https://doi.org/10.1080/17415977.2016.1161034

53. Seidl DT, Oberai AA, Barbone PE. The Coupled Adjoint-State Equation in forward and inverse linear elasticity: Incompressible plane stress. *Comput Methods Appl Mech Eng*. 2019;357. https://doi.org/10.1016/j.cma.2019.112588

54. Tikhonov AN. Solution of Incorrectly Formulated Problems and the Regularization Method. *Soviet Mathematics Doklady*, 1963; 4, 1035-1038.

55. Samani A, Plewes D. A method to measure the hyperelastic parameters of ex vivo breast tissue samples. *Phys Med Biol*. 2004;49(18):4395-4405. https://doi.org/10.1088/0031-9155/49/18/014

56. Boussinesq J (1842-1929). A du texte. Application des potentiels à l'étude de l'équilibre et du mouvement des solides élastiques, principalement au calcul des déformations et des pressions que produisent, dans les solides, des efforts quelquonques exercés sur une petite partie de leur surface ou de leur intérieur : mémoire suivi de notes étendues sur divers points de physique mathématique et d'analyse /par J.Boussinesq, 1885. Accessed March 8, 2021. https://gallica.bnf.fr/ark:/12148/bpt6k9651115r

57. Polak E, Ribiere G. Note sur la convergence de méthodes de directions conjuguées. *Rev Française d'informatique Rech opérationnelle Série rouge*. 1969;3(16):35-43. https://doi.org/10.1051/m2an/196903r100351

58. Strutz T. *Data Fitting and Uncertainty (A Practical Introduction to Weighted Least Squares and Beyond)*. Springer Vieweg; 2016.

59. Szabo TL. *Diagnostic Ultrasound Imaging: Inside Out: Second Edition*. Elsevier Inc.; 2004. https://doi.org/10.1016/C2011-0-07261-7

60. Timoshenko SP, Goodier JN, Abramson HN. Theory of Elasticity (3rd ed.). *J Appl Mech*. 1970;37(3):888-888. https://doi.org/10.1115/1.3408648

61. Mehrabian H, Samani A. An iterative hyperelastic parameters reconstruction for breast cancer assessment. *Med Imaging 2008 Physiol Funct Struct from Med Images*. 2008;6916(March 2008):69161C. https://doi.org/10.1117/12.770971

62. Mousavi SR, Rivaz H, Sadeghi-Naini A, Czarnota GJ, Samani A. Breast ultrasound elastography using full inversion-based elastic modulus reconstruction. *IEEE Trans Comput Imaging*. 2017;3(4):774-782. https://doi.org/10.1109/tci.2017.2741422

63. Samani A, Zubovits J, Plewes D. Elastic moduli of normal and pathological human breast tissues: an inversion-technique-based investigation of 169 samples. *Physics Med Biol*. 2017;52:1565-1576. https://doi.org/10.1088/0031-9155/52/6/002

64. Alam SK, Ophir J. Reduction of signal decorrelation from mechanical compression of tissues by temporal stretching: applications to elastography. *Ultrasound Med Biol*. 1997;23(1):95-105. https://doi.org/10.1016/s0301-5629(96)00164-0. PMID: 9080622.

65. Konofagou E, Ophir J. A new elastographic method for estimation and imaging of lateral displacements, lateral strains, corrected axial strains and Poisson's ratios in tissues. *Ultrasound Med Biol*. 1998;24(8):1183-99. https://doi.org/10.1016/s0301-5629(98)00109-4. PMID: 9833588.

66. Lopata RG, Nillesen MM, Hansen HH, Gerrits IH, Thijssen JM, de Korte CL. Performance evaluation of methods for two-dimensional displacement and strain estimation using ultrasound radio frequency data. *Ultrasound Med Biol*. 2009;35(5):796-812. https://doi.org/10.1016/j.ultrasmedbio.2008.11.002. Epub 2009 Mar 17. PMID: 19282094.

67. Lee WN, Provost J, Fujikura K, Wang J, Konofagou EE. In vivo study of myocardial elastography under graded ischemia conditions. *Phys Med Biol*. 2011;56(4):1155-72. https://doi.org/10.1088/0031-9155/56/4/017. Epub 2011 Feb 1. PMID: 21285479; PMCID: PMC4005801.

68. Zhang Y, Sun T, Teng Y, Li H, Kang Y. Fast axial and lateral displacement estimation in myocardial elastography based on RF signals with predictions. *Biomed Mater Eng*. 2015;26 Suppl 1:S1633-9. https://doi.org/10.3233/BME-151462. PMID: 26405928.

69. Techavipoo U, Chen Q, Varghese T, Zagzebski JA. Estimation of displacement vectors and strain tensors in elastography using angular insonifications. *IEEE Trans Med Imaging*.

APPENDIX: DERIVATION OF EQUATION 10

According to Hooke's law:

$$\begin{bmatrix} \varepsilon_{11} \\ \varepsilon_{22} \\ \varepsilon_{33} \\ \gamma_{23} \\ \gamma_{13} \\ \gamma_{12} \end{bmatrix} = \frac{1}{E} \begin{bmatrix} 1 & -\nu & -\nu & 0 & 0 & 0 \\ -\nu & 1 & -\nu & 0 & 0 & 0 \\ -\nu & -\nu & 1 & 0 & 0 & 0 \\ 0 & 0 & 0 & 2+2\nu & 0 & 0 \\ 0 & 0 & 0 & 0 & 2+2\nu & 0 \\ 0 & 0 & 0 & 0 & 0 & 2+2\nu \end{bmatrix}$$

$$\times \begin{bmatrix} \sigma_{11} \\ \sigma_{22} \\ \sigma_{33} \\ \sigma_{23} \\ \sigma_{13} \\ \sigma_{12} \end{bmatrix} \tag{A1}$$

Here, indices 1, 2, and 3 pertain to x, y, and z coordinates, respectively. The above leads to the following for $\begin{bmatrix} \varepsilon_{yy} \\ \varepsilon_{zz} \end{bmatrix}$:

$$\begin{bmatrix} \varepsilon_{yy} \\ \varepsilon_{zz} \end{bmatrix} = \begin{bmatrix} \varepsilon_{22} \\ \varepsilon_{33} \end{bmatrix} = \frac{1}{E} \begin{bmatrix} -\nu & 1 & -\nu & 0 & 0 & 0 \\ -\nu & -\nu & 1 & 0 & 0 & 0 \end{bmatrix}$$

$$\times \begin{bmatrix} \sigma_{11} \\ \sigma_{22} \\ \sigma_{33} \\ \sigma_{23} \\ \sigma_{13} \\ \sigma_{12} \end{bmatrix} \tag{A2}$$

E and ν in terms Lame' parameters are as follows:

$$E = \frac{\mu(3\lambda + 2\mu)}{\lambda + \mu} \text{ and } \nu = \frac{\lambda}{2(\lambda + \mu)}$$

Substituting the above in A2 leads to:

$$\begin{bmatrix} \varepsilon_{yy} \\ \varepsilon_{zz} \end{bmatrix} = \begin{bmatrix} \dfrac{-\lambda}{2\mu(3\lambda + 2\mu)} & \dfrac{\lambda + \mu}{\mu(3\lambda + 2\mu)} & \dfrac{-\lambda}{2\mu(3\lambda + 2\mu)} \\ \dfrac{-\lambda}{2\mu(3\lambda + 2\mu)} & \dfrac{-\lambda}{2\mu(3\lambda + 2\mu)} & \dfrac{\lambda + \mu}{\mu(3\lambda + 2\mu)} \end{bmatrix}$$

$$\times \begin{bmatrix} \sigma_{xx} \\ \sigma_{yy} \\ \sigma_{zz} \end{bmatrix} \tag{A3}$$